Biology of Reproduction, 2018, 99(5), 1045–1056
doi:10.1093/biolre/ioy119
Research Article
Advance Access Publication Date: 18 May 2018

OXFORD

Research Article

Porphyromonas gingivalis strain-dependent inhibition of uterine spiral artery remodeling in the pregnant rat†

Priscilla Phillips[1], Mary B. Brown[2,‡], Ann Progulske-Fox[3,‡], Xiao-Jun Wu[4] and Leticia Reyes[4,*]

[1]Department of Microbiology & Immunology, A.T. Still University of Health Sciences, Kirksville College of Osteopathic Medicine, Kirksville, Missouri, USA; [2]Department of Infectious Disease and Immunology, College of Veterinary Medicine and D. H. Barron Reproductive and Perinatal Biology Research Program, University of Florida, Gainesville, Florida, USA; [3]Center for Molecular Microbiology and Department of Oral Biology, College of Dentistry, University of Florida, Gainesville, Florida, USA and [4]Department of Pathobiological Sciences, University of Wisconsin–Madison, School of Veterinary Medicine, Madison, Wisconson, USA

*__Correspondence:__ Department of Pathobiological Sciences, University of Wisconsin–Madison, School of Veterinary Medicine, 2015 Linden Drive, Madison, WI 53706, USA. Tel: +608-263-7884; Fax: 608-263-0438; E-mail: lreyes2@wisc.edu
‡These authors contributed equally to this work.

†__Grant Support:__ Research reported in this publication was supported by the Eunice Kennedy Shriver National Institute of Child Health & Human Development of the National Institutes of Health under Award Number R15HD081439. The content is solely the responsibility of the authors and does not necessarily represent the official views of the National Institutes of Health.
Edited by Dr. Romana Nowak, PhD, University of Illinois

Received 10 January 2018; Revised 24 April 2018; Accepted 16 May 2018

Abstract

Porphyromonas gingivalis (*Pg*) is an important periodontal pathogen that is also implicated in pregnancy complications involving defective deep placentation (DDP). We hypothesized that *Pg* invasion of the placental bed promotes DDP. Pregnant rats were intravenously inoculated with sterile vehicle, *Pg* strain W83, or A7436 at gestation day (GD) 14 (acute cohort). Nonpregnant rats received repeated oral inoculations for 3 months before breeding (chronic cohort). Tissues and/or sera were collected at GD18 for analysis. *Pg* infection status was determined by seroconversion (chronic cohort) and by presence of *Pg* antigen in utero-placental tissues processed for histology and morphometric assessment of spiral artery remodeling. Mesometrial tissues from seropositive dams were analyzed for expression of interleukin 1β, 6, and 10, TNF, TGF-β, follistatin-related protein 3, and inhibin beta A chain since these genes regulate extravillous trophoblast invasion. The in situ distribution of W83 and A7436 antigen in utero-placental tissues was similar in both cohorts. In the acute cohort, mesometrial stromal necrosis was more common with W83, but arteritis was more common with A7436 infection ($P < 0.05$). Increased vascular necrosis was seen in mesometrium of chronically infected groups ($P < 0.05$). Only A7436-infected animals had increased fetal deaths, reduced spiral artery remodeling, reduced inhibin beta A expression, and an increased proportion of FSLT3 positive extravillous trophoblasts within spiral arteries. While infection with both Pg strains produced varying pathology of the deep placental bed, only infection with strain A7436 resulted in impaired spiral artery remodeling.

Summary Sentence

Invasion of the placental bed by *Porphyromonas gingivalis* impairs spiral artery remodeling and increases fetal loss in a microbial strain-dependent manner.

Key words: spiral artery, metrial triangle, *Porphyromonas gingivalis*, rat pregnancy.

Introduction

Defective deep placentation (DDP) is defined as inadequate physiologic remodeling of the deep myometrial segments of the uterine spiral arteries [1]. DDP is a common disorder of various pregnancy complications with detection rates ranging between 48 and 83% of first and second trimester spontaneous abortions, 35% of preterm premature rupture of membranes, 34% of spontaneous preterm births, 58% of abruption placentae, 48% of intrauterine growth restriction (IUGR), and 73% of preeclampsia cases [2]. Uterine arteries that have failed to be remodeled during pregnancy may also exhibit uterine atherosis, a late pregnancy lesion that is characterized by peri-vascular infiltrates of foam filled macrophages and lymphocytes with fibrinoid necrosis and thrombosis of the vessel [1].

Optimal remodeling of the uterine spiral arteries involves loss of their elasticity and conversion to large dilated vessels that allow for efficient blood flow to the placenta. This process is highly regulated and thought to occur in various stages whereby the integrity of the arterial endothelium and the surrounding vascular smooth muscle layer are disrupted and invaded by extravillous trophoblasts (EVT). The first stage of remodeling begins during decidualization of the uterus and is characterized by disruption of the arterial endothelium and intimal layer and by loss of vascular smooth muscle cells [3, 4]. The second stage of remodeling involves invasion of the arterial lumen and the uterine interstitium by EVT [5]. Disruption at any stage of this process can result in varying degrees of DDP with subsequent damage to the placenta and/or fetal morbidity.

There is emerging evidence that defective decidualization during early pregnancy can affect EVT invasion and spiral artery remodeling resulting in pregnancy complications that involve DDP [4, 6]. A plethora of cytokines within the uterine microenvironment such as IL-1β, IL-6, IL-10, IL-11, IL-15, TNF-α, and the transforming growth factor beta (TGF-β) superfamily including the activins regulate EVT invasion and spiral artery remodeling during normal pregnancy [7–11]. Derangements in some of these factors have been shown to inhibit EVT invasion in vitro or disrupt implantation and placentation in vivo [11–14]. It is notable that periodontal bacteria, which have been detected in the placenta of women with preeclampsia [15–17], can elicit cytokine and chemokine responses from decidual cells [18] that could reduce EVT invasion and spiral artery remodeling [11]. Indeed, TNF-α-mediated inflammation triggered by lipopolysaccharide inhibits spiral artery remodeling and promotes fetal growth restriction and preeclampsia-like disease in rats [14].

Porphyromonas gingivalis (Pg) is an important Gram-negative periodontal pathogen of humans that is also implicated in promoting cardiovascular disease [19], low birth weight, IUGR, preeclampsia, and spontaneous preterm birth [15–17, 20–26]. In women with complicated pregnancies, the rate of detection of *Pg* DNA or antigen within the uterine compartment ranges between 30 and 92% [15–17, 22, 25]. Experimental infection in rodents and rabbits have shown that *Pg* strains A7436 and W83 can invade the placenta and/or fetus via hematogenous routes and induce placental vascular defects, enhanced expression of pro-TH1 type cytokines (IFN-γ, IL-2, IL-12, and TNF-α), fetal growth restriction, and spontaneous preterm delivery [27–30]. However, a confounding aspect of these studies is that the variety of adverse pregnancy outcomes associated with *Pg* infection involve different underlying pathologies. For instance, preeclampsia and fetal growth restriction are usually manifestations of abnormal placentation that began during the first trimester of pregnancy [5]. In contrast, spontaneous preterm birth usually takes place during the second or third trimester of pregnancy and is often the result of an overt inflammatory response involving the placenta, chorioamnion, or choriodecidua [31]. Although these complications arise from diverse pathologies within the placenta or chorioamnion, one common pathologic feature of these disorders is DDP, which occurs within the maternal side of the maternal–fetal interface [32, 33].

While in vitro studies using the immortalized first trimester EVT cell line HTR8/SVneo cells suggest *Pg* may have the capacity to affect spiral artery remodeling [34, 35], this has never been determined in vivo. Given that *Pg* invasion of the maternal–fetal interface [15, 17, 25] is linked to pregnancy complications that often have DDP [1, 32], we hypothesized that some *Pg* strains interfere with the physiologic remodeling of the uterine spiral arteries. We focused our analysis on *Pg* strains A7436 and W83 since these strains induce a diverse range of pregnancy complications in rodents [27–30, 36] linked to DDP in women [1, 32, 37]. Namely, experimental infection with W83 induces preterm delivery and fetal growth restriction in rodents [29, 30], whereas A7436 induces placentitis, uterine vasculitis [36], and fetal growth restriction [27, 28].

In this study, we have demonstrated that *Pg* delivered intravenously or by repeated oral inoculations is able to reach the maternal–fetal interface in rats. While both *Pg* strains could be found in association with decidual and mesometrial stromal cells, only *Pg* strain A7436 reduced uterine spiral artery remodeling with an increased number of embryonic deaths. This lesion was associated with derangements in inhibin βA expression, which is important in decidualization and may reflect decidual dysfunction.

Materials and methods

Animals

All procedures were conducted after approval from the University of Florida, and the University of Wisconsin Institutional Animal Care and Use Committees. All experiments used specific pathogen-free Sprague Dawley (SD) rats (Charles River International Laboratories, Inc., Kingston, NY). Animals were housed in the same room under barrier conditions. In all experiments, control animals were always handled before infected animals. Each experiment used a Latin square design so that an equal number of animals were assigned to each treatment group. Specimens collected from two independent experiments were used to establish reproducibility.

Acute infection

Archived tissues from a previous study [36] were used to assess acute changes within the placental bed. In this study, pregnant rats received

one intravenous inoculation of 10^5, 10^7, or 10^9 colony-forming units (CFU) of *Pg* strain W83 or A7436 at gestation day (GD) 14, before invasion by interstitial trophoblasts [38]. Dams were euthanized 4 days later (GD18) when interstitial trophoblast invasion is at its peak [39]. Utero-placental tissues were collected for histology.

Chronic infection

An oral inoculation protocol was used to establish a chronic periodontal infection in rats [40]. Six- to eight-week-old female rats first received kanamycin (20 mg) and ampicillin (20 mg) daily for 4 days in the drinking water to reduce the number of commensal bacteria. The oral cavity was then swabbed with 0.12% chlorhexidine gluconate (Peridex: 3M ESPE Dental Products, St Paul, MN, USA) mouth rinse to inhibit the endogenous organisms and to promote subsequent colonization with *Pg*. Rats were switched back to antibiotic free water and rested for 3 days to allow clearance of antibiotics from their system before beginning the inoculation phase of the study. An equal number of rats were randomly assigned to control, *Pg* W83, or A7436 groups. Each *Pg* strain was mixed in sterile 2% (w/v) low viscosity carboxymethylcellulose (CMC; Sigma, St Louis, MO, USA) at a concentration of 1×10^{10} bacteria CFU per ml. Each animal received an oral inoculation containing 1×10^9 CFU for 4 consecutive days per week on 6 alternate weeks totaling 24 inoculations over a 12-week period. Control animals received sterile 2% CMC. During the inoculation period, animals were fed a gamma-irradiated powdered rodent diet (Teklad Global 18% protein rodent diet, Envigo, Madison, WI) in order to minimize disruption of bacterial plaque. At the end of the inoculation period, rats were switched back to the same diet in a pelleted form and rested for 1 week before breeding. Breeding was confirmed by the presence of sperm in vaginal lavages that were performed the following morning, which was considered GD0. Dams were euthanized at GD18; all fetuses were weighed and recorded. Utero-placental units were randomly selected for histology or gene expression analysis irrespective of fetal weight. Dam sera was collected for detection of *Pg*-specific IgM and IgG.

Cultivation and preparation of bacteria

Pg W83 and A7436 were grown on supplemented Tryptic Soy broth and agar as previously described [41]. CFU were estimated by optical density readings taken at 550 nm. Broth cultures were pelleted by centrifugation at 12,000× *g* for 4 min at room temperature and resuspended in sterile 2% (w/v) low CMC. The CFU of bacterial suspension was confirmed by culture as previously described [41].

Tissue selection and processing

At time of necropsy, fetuses were removed from the placenta. The utero-placenta was fixed intact for 24 h at 4°C in freshly prepared 0.25% paraformaldehyde-0.2 mol/L lysine-0.02 mol/L sodium periodate [36]. Specimen selection of archived tissues was based on initial evaluation of hematoxylin and eosin (H&E) stained sections that showed an intact mesometrial triangle at the center of the utero-placental unit as indicated by the presence of the central artery.

In the chronic infection study, fetuses were removed from the placenta. Excess uterine tissue was trimmed from the mesometrial triangle that was left attached to the placenta. In order to avoid over fixation of the tissue, the entire utero-placenta was fixed in 10% buffered formalin for 24 h at room temperature, washed in distilled water and transferred to 70% ethanol until trimming. At trimming, the uterus/placenta was carefully transected through the center so that both mesometrial triangle and placenta could be evaluated. Both sections were embedded in paraffin as previously described [25] and stained with H&E for initial histologic evaluation. Utero-placental specimens with presence of the maternal channel (MC) that were also confirmed to be positive for *Pg* antigen were used for morphometric analysis.

Mesometrial tissues selected for gene expression analysis were aseptically peeled away from the placenta at time of necropsy. Excess uterine tissue (not part of the mesometrial triangle/decidua basalis) was removed. Mesometrial tissue was immersed in TRIzol reagent (Life Technologies, Grand Island, NY) prior to flash freezing in liquid nitrogen. Frozen tissues were stored at –80°C until RNA extraction.

Immunofluorescent histology

Five micron thick paraffin embedded sections were mounted onto glass plus slides and processed for antibody staining as previously described [42]. *Pg* antigen was detected with a rabbit polyclonal antibody to whole *Pg* W83 (diluted 1:2000) that was previously shown to be specific for *Pg* but also able to detect other *Pg* strains with equivalent avidity [25, 41]. Preimmunized rabbit serum was used as an isotype control. Remaining antibodies used in this study are commercially available and validated for use in paraffin embedded tissues. Details of all antibodies used in this study are summarized in Supplementary Table S1. All commercial antibodies were used at a dilution of 1:200. Trophoblasts were detected with anti-cytokeratin 7 mouse monoclonal antibody clone LP1K (Abcam, Cambridge, MA). Endothelial cells were detected with rabbit polyclonal antibody to CD31 (Abbiotec, San Diego, CA). Smooth muscle cells were identified with anti-α-actin mouse clone 1A4 (Biorad Laboratories, Hercules, CA). Goat anti-mouse or anti-rabbit labeled with ALEXA 594 (absorption 590, emission 617) or with ALEXA 647 (absorption 650, emission 665) (Life Technologies, Grand Island, NY) were used as secondary antibodies. Isotype antibody staining of corresponding tissue sections were included in all experiments in order to define nonspecific binding. ActinGreen 488 was used as a general cell stain and cell nuclei were stained with DAPI (Life Technologies, Grand Island, NY).

Histologic assessment of mesometrial lesions and morphometry of antibody stained sections

At least two utero-placental sections of each specimen (n = 5) were evaluated. All sections were examined with an EVOS FL Auto Cell Imaging System (Life Technologies, Grand Island, NY). Only specimens in which the central channel/artery was present were used for evaluation and morphometric analysis. Specimens from control animals were first evaluated to establish normal histology. Specimens from *Pg*-infected animals were de-identified and coded prior to evaluation and morphometric analysis. A specimen was considered positive for stromal necrosis, arteritis, and/or coagulative necrosis if the lesion was detected in at least one tissue section per slide. Stromal necrosis referred to regions of the decidual stroma with cellular debri and pyknotic nuclei that was sometimes apposed with a margin of macrophages and/or neutrophils (Supplementary Figure S1A). Arteritis was considered present if macrophages, lymphocytes, or neutrophils were observed invading and/or surrounding the blood vessel wall (Supplementary Figure S1B). In the chronic infection cohort, arteritis was characterized by fibrinoid necrosis with macrophages and lymphocytes infiltrating the vessel wall (Supplementary Figure S1C). Sections were considered to have coagulative necrosis if vessel architecture was retained but there was loss of nuclei (Supplementary Figure S1E) [43]. Specimens that contained

foci of liquefactive necrosis that was contiguous with coagulative necrosis were still assigned to the coagulative necrosis group.

For morphometric analysis of immunostained sections, several images that covered the entire span of the decidua basalis were taken with the EVOS FL Auto Cell Imaging System (Life Technologies, Grand Island, NY) that has UPlanAPO objectives (Olympus, Waltham, MA). Filters used for fluorescent imaging were Texas Red, Cy5, and DAPI light cubes (Life Technologies, Grand Island, NY). During image capture of fluorescent stained sections, camera settings were optimized using the tissue section with the highest degree of fluorescent signaling. Once image capture settings were established, the same settings were used for all the tissues within the specific labeling experiment. Images were saved as 8-bit tiff files with a resolution of 72 pixels/inch. For publication purposes, image resolution was increased to 300 or 400 dpi with Adobe Photoshop version 19 CC (Adobe). For qualitative assessment of immunostained sections, the scan feature of the EVOS system (Life Technologies, Grand Island, NY) was used to stitch together a series of images taken at 10× magnification that spanned the entire utero-placental unit.

Calibrated digital images were analyzed with Image J 1.50b analysis software (Rasband, National Institutes of Health, USA). Morphometry of spiral artery remodeling was performed with the particle analysis feature. Trophoblast invasion was determined by dividing the average area (mm^2) of cytokeratin positive staining within an image by the total area of the mesometrial triangle of the same image. Loss of endothelium and vascular smooth muscle was assessed by manually tracing the arterial segments within the mesometrial triangle of each CD31/smooth muscle actin labeled vessel excluding the vessel lumen. The traced area of the vessel was deemed the total area. Particle analysis was used to measure the CD31 and α-actin positive area within the area of the traced vessel. The percent area of all arterial segments within the mesometrial triangle of two sections per biological replicate was determined. Final area measurements of each biological replicate were then averaged and reported as the mean percent area (mm^2).

Placental morphometry of H&E sections that contained the MC was performed on stitched composite images taken at 4× magnification (Supplementary Figure S2). A calibrated image taken at 4× magnification was used to as a reference to set the scale of one tile within each composite image. After the composite image was calibrated, the edge of the placenta (spongiotrophoblast and labyrinth) was manually traced and the area was determined with Image J 1.50b analysis software (Rasband, National Institutes of Health, USA).

Colocalization of follistatin-related protein 3 and cytokeratin-7 was performed on uteroplacental specimens from control and *Pg*-infected groups. Immunofluorescent stained images that spanned the entire region of the mesometrial triangle of each specimen were used for the analysis. Data from all images obtained from the same biological replicate were added before determining percentage of follistatin-related protein 3 positive EVT [i.e., the total number of follistatin-related protein 3 positive EVT (cytokeratin-7 positive cells) divided by the total number of EVT (both follistatin-related protein 3 negative and positive cells)].

Detection of *Pg*-specific IgM and IgG

Dam antibody responses to *Pg* were determined by ELISA as previously described [44]. Whole cell *Pg* lysate was further homogenized by sonication (Sonic Dismembrator, Thermo Fisher Scientific, Waltham, MA) and the total protein concentration of the lysate was measured by Bradford Protein Assay (Thermo Fisher Scientific, Waltham, MA). Stock aliquots of *Pg* lysates were stored at a concentration of 2 mg/ml at –20 C. For the ELISA assay, *Pg* lysates were diluted with 50 mM bicarbonate coating buffer pH 9.4 (Thermo Fisher Scientific, Waltham, MA) to yield a final concentration of 20 μg/ml. Goat anti-rat IgM (Southern Biotech, Birmingham, AL) and donkey anti-rat IgG (Thermo Fisher Scientific, Waltham, MA), both conjugated to horse radish peroxidase, were used for detection (1:4000 and 1:2500, respectively). Pooled sera from *Pg*-infected dams and uninfected control animals were used to establish serum dilutions that fell within the linear range of a dilution curve. Subsequent ELISAs were batched and each plate contained a positive and negative control. In order to minimize plate to plate variation, each 96 well plate contained serum samples from each group. All samples were run in duplicate and readings were obtained with a Model 680 microplate reader (Biorad Laboratories, Hercules, CA).

Gene expression analysis

RNA from mesometrial tissues was extracted according to the manufacturers' protocol (TRIzol reagent, Life Technologies, Grand Island, NY). Mesometrial tissues were minced in TRIzol at a ratio of 70 to 150 mg of tissue in 1 ml of reagent followed by homogenization with a Read Mill 4 homogenizer (Thermo Fisher Scientific, Waltham, MA). RNA quality and quantity were assessed by Nanodrop electrophoresis (Agilent RNA 6000, Agilent Technologies, Inc., Santa Clara, CA). *Il1b, Il6, Il10, Tnf, Tgfb1, Fstl3, Inhba*, and *Actb* expression were measured by RT-qPCR using Quantitect primers (Qiagen Inc., Germantown, MD) using the manufacturer's reagents and protocols. Reactions were performed in duplicate with Light Cycler 96 (Roche Applied Science, Indianapolis, IN). Relative gene expression for each specimen was determined by the comparative C_t method with β-actin used as the reference and values reported as $2^{-(\Delta Cq)}$ [45].

Fetal sex determination

PCR-based detection of the male *Sry1* gene [46] was used to determine fetal sex in formalin fixed paraffin-embedded specimens used for morphometric analysis (Supplementary Table S2 and Figure S3). Genomic DNA from uteroplacental specimens was extracted using ReliaPrep FFPE gDNA Miniprep System according to manufacturer instructions (Promega, Madison, WI). PCR-based amplification of the beta actin gene (*Actb*) was used to assess DNA quality of each sample. For all PCR reactions, the denaturing step was performed at 95°C for 3 min, 35 amplification cycles were done at 95°C for 30 s, 57°C for 45 s, and 72°C for 1 min, and the final annealing step was done at 72°C for 5 min with a T100 Thermal cycler (BioRad Laboratories, Hercules, CA).

Statistical analysis

Frequency measurements were analyzed by the Chi-square test. Gene expression data and morphometry measurements were analyzed by one-way analysis of variance (ANOVA) followed by Tukey multiple comparison test if ANOVA indicated a significant difference among group means. Raw data measurements were transformed prior to ANOVA testing if Bartlett test showed that variances were significantly different among groups. Nonparametric data were analyzed by Kruskall–Wallis and Dunn test. Testing was performed with Prism 7.03 Software (GraphPad). For all testing, $P < 0.05$ was considered significantly different.

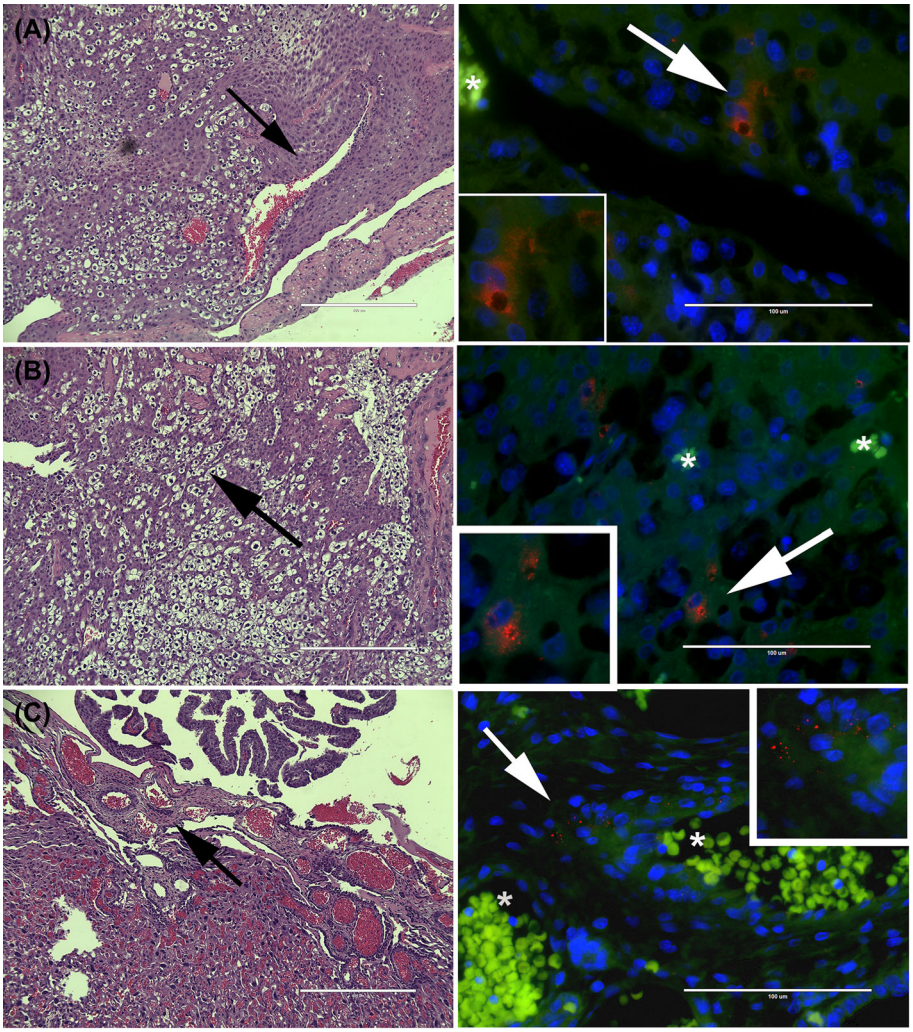

Figure 1. Representative images of *Pg* antigen in the mesometrial triangle and chorionic plate of *Pg* W83 (A) or *Pg* A7436 (B and C) infected dams. Left panels are H&E-stained sections that correspond to microbial location within the tissue (black arrows) shown on the right. *Pg* W83 (A) and *Pg* A7436 (B) antigen were primarily located in mesometrial stromal cells. Panel C is a representative image of A7436 but both strains were found in the chorionic plate. *Pg* antigen is pseudo-colored red, host cells pseudo-colored green, and nuclei pseudo-colored blue. "$*$" indicates the presence of autofluorescent red blood cells within the vessel lumen. Magnified inserts are highlighted regions (white arrows). All scale bars are equivalent to 1000 μm.

RESULTS

In situ detection of *Pg* in utero-placental tissues

Since our primary interest was to determine the impact of intra-uterine invasion with *Pg*, we screened utero-placental tissue sections for the presence of microbial proteins using a rabbit polyclonal antibody to whole cell W83 (Figure 1) [41]. *Pg* antigen was not detected in any tissues from control animals (Supplementary Figure S4). In both acute and chronic infection cohorts, *Pg* antigen was most often observed in the mesometrial and decidual stroma in animals infected with either *Pg* strain (Figure 1A). The distribution of *Pg* antigen was usually focal or multifocal and appeared to be internalized in some cells or in the extracellular matrix. *Pg* antigen was also present within the mesenchyme layer of the chorionic plate (Figure 1C). In the acute infection cohort, *Pg* was detected in utero-placental specimens from rats infected with W83 (70% positive) or A7436 (64% positive). In the chronically infected cohort, 75% of utero-placental units from W83-infected dams and 81% of tissues from A7436-infected dams were positive for *Pg* antigen in the mesometrial and/or placental compartments. Specimens that were positive for Pg antigen were used for subsequent analysis.

Dam antibody responses to *Pg*

In order to determine if chronically infected animals developed an immune response to *Pg*, sera collected at time of necropsy were assayed for the presence of *Pg*-specific IgM and IgG. There was no difference in the amount of anti-*Pg* IgM among the groups (data not shown). However, four of six W83 inoculated dams and five of seven A7436 inoculated dams had a significant increase in the amount of *Pg* specific IgG based on absorbance values ($P < 0.0001$, Supplementary Figure S5). Only tissues from dams that seroconverted were used for gene expression analysis.

Impact of *Pg* infection on the placental bed and fetus

Stromal and coagulative necrosis was observed in all treatment groups regardless of duration of infection (Table 1). However, in the acute infection group, the prevalence of stromal necrosis was greater

Table 1. Proportion of lesions detected within the mesometrial triangle of sham control, acute, and chronically infected dams positive for Pg antigen.

Acute infection	Stromal necrosis[1]	Arteritis[1]	Coagulative necrosis[1]
Control	1/12 (8%)[a]	0/12 (0%)[a]	4/12 (33%)
W83	4/7 (57%)[a]	2/7 (29%)	1/7 (14%)
A7436	1/7 (14%)	4/7 (57%)[a]	1/7 (14%)
Chronic infection	**Stromal necrosis**	**Arteritis**	**Coagulative necrosis**
Control	4/13 (31%)	0/13 (0%)	5/13 (38%)[ab]
W83	2/6 (38%)	0/6 (0%)	5/6 (83%)[a]
A7436	3/9 (33%)	2/9 (22%)	8/9 (89%)[b]

[1]Values within each column that have the same superscript (a or b) are different by Chi-Square analysis ($P < 0.05$).

in W83-infected animals than in controls ($P < 0.05$, Table 1). Although arteritis was exclusively present in *Pg*-infected animals, the number of Pg A7436 positive tissues was significantly greater than in control tissues but not in W83-infected tissues (Table 1).

In the chronically infected group, there was no difference in the frequency (Table 1) or the overall amount (data not shown) of stromal necrosis among treatment groups. While none of the control or W83 groups in this cohort had arteritis, two A7436 positive specimens had atherosis-like pathology within the mesometrial triangle that consisted of fibrinoid necrosis of the vessel wall with invasion by mononuclear leukocytes (Supplementary Figure S1C). Partial EVT invasion of these arteries was also evident (Supplementary Figure S1C). A greater proportion of W83 and A7436 positive tissues had coagulative necrosis with or without liquefactive necrosis than did controls (Table 1). Coagulative necrosis was most commonly found at the mesometrial/decidual junction (Supplementary Figure S1D). Liquifactive necrosis was never seen without coagulative necrosis in any of the specimens.

In our assessment of the chorionic plate and umbilical cord, we did not find inflammatory cell infiltrates in any of the *Pg*-positive sections that were evaluated from either the acute or chronic cohort (Supplementary Figure S6).

Since *Pg* has been shown to increase embryonic lethality and promote fetal growth restriction [27, 28], we compared placental size, fetal weight, litter size, and number of fetal resorptions from control and *Pg*-positive animals (i.e., *Pg*-positive utero-placental tissues and/or dams that seroconverted postinoculation) (Table 2). Placental size and corresponding fetal weight measurements were limited to specimens that were selected for morphometry based on criteria described in Methods. Statistical analysis of litter size and resorption number per litter was performed on data from *Pg*-inoculated dams that seroconverted. We found that placental specimens positive for A7436 were smaller than controls but not smaller than the W83 (Table 2). There was no difference between placental size of W83 positive and control tissues. There was no difference in corresponding fetal weights or litter size among the groups. However, dams seropositive for A7436 had a greater number of fetal resorptions than controls (Table 2). While the proportion of fetal resorptions in A7436-infected dams was greater than W83-infected animals, it did not attain statistical significance.

Fetal resorptions were also evaluated by histology (Supplementary Figure S7). Regardless of treatment group, pathologic features of resorptions were qualitatively similar in all groups. All specimens had varying degrees of mesometrial decidualization with mild to moderate vascular necrosis in the myometrium. Necrosis of the placenta was present in all groups, but was more extensive in specimens from *Pg*-infected animals.

Pg A7436 infection reduces spiral artery remodeling

Utero-placental specimens found to be positive for *Pg* and sham controls were examined for remodeling of the uterine spiral artery. We first measured the extent of EVT invasion into the mesometrial triangle since this event begins at GD15 and peaks at GD18 [39] and would allow us to investigate this process in both acute and chronically infected cohorts (Figure 2; Supplementary Figure S8). EVT invasion into W83 positive tissues was not significantly different from control tissues in either the acute or chronically infected cohort (Figure 2A and B). On the other hand, A7436-positive tissues from both cohorts showed a significant reduction in EVT invasion compared to W83-infected and control groups ($P < 0.05$). There was no fetal sex difference in the extent of EVT invasion in any of the treatment groups (data not shown).

Tissues from the chronically infected cohort were evaluated for earlier changes in spiral artery remodeling that began before GD14. Namely, we measured the amount of endothelial (Figure 3A; Supplementary Figure S8) and vascular smooth muscle cells retained within the mesometrial spiral arteries (Figure 3B) [47]. Tissues from W83-infected dams had the same degree of endothelial and vascular smooth muscle cell loss as the control group. In contrast, tissues from A7436-infected animals showed a significant retention of both mesometrial arterial endothelium and smooth muscle cells that indicated reduced remodeling of these vessels ($P < 0.001$). There was no fetal sex difference in the extent of endothelial retention or vascular smooth muscle among the groups (data not shown).

Pg-induced dysfunction of spiral arterial remodeling is not associated with mesometrial inflammation but is linked to dysregulation of decidual inhibin βA expression

Experimental infection with *Pg* can modulate the production of IL-1β, IL-6, IL-10, and TNF-α at the maternal–fetal interface in rodents [28, 29]. These cytokines have been shown to affect spiral artery remodeling in the rat or EVT invasion in vitro [14, 48]. Therefore,

Table 2. Impact of chronic *Pg* infection on fetal outcomes.

Group	Placental size[1] (mm^2) Mean ± SD[3]	Fetal weight[1] (gm) Mean ± SD	Litter Size[2] Mean ± SD	Resorptions[2] Number +/total (%)[3]
Control	41.0 ± 7.3[a]	1.52 ± 0.15	12.0 ± 1.7	4/73 (5)[a]
W83	34.5 ± 2.4	1.62 ± 0.18	11.5 ± 1.1	6/60 (10)
A7436	31.2 ± 3.8[a]	1.56 ± 0.16	11.8 ± 1.5	14/67 (21)[a]

[1]Values are only from specimens that were used for morphometry (n = 6 uteroplacentas and n = 6 corresponding fetuses per group).
[2]Values were obtained from all control and *Pg*-infected dams that seroconverted (n = 5 dams for control, n = 4 dams for W83, and n = 5 dams for A7436).
[3]Values within each column that have the same superscript (a) are different by ANOVA and Tukey test ($P < 0.05$).

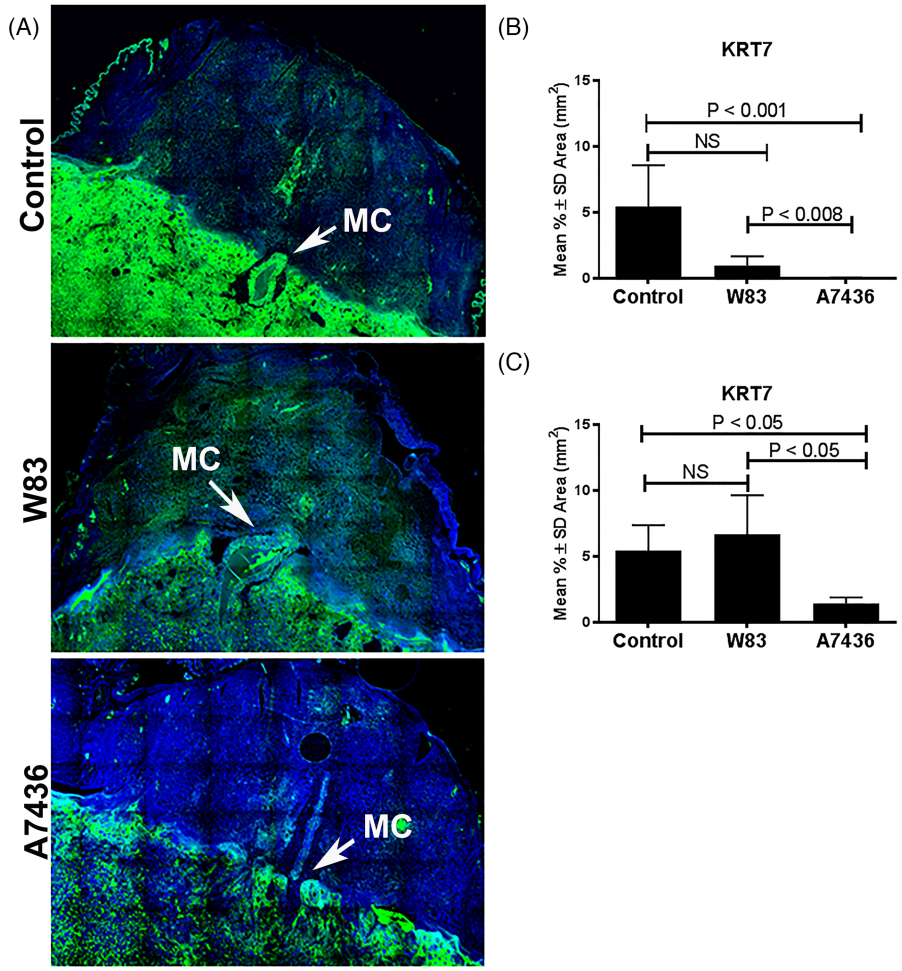

Figure 2. *Pg* strain-dependent effects on EVT invasion into the mesometrial triangle at GD18 from acute and chronic infection cohorts. Panel A shows representative images of EVT (green) invasion into the mesometrial triangle of control tissues and *Pg* W83 or *Pg* A7436-infected tissues. EVT cells (green) were stained with anti-cytokeratin 7 (KRT7); nuclei (blue) were stained with DAPI. Images are 10× magnified image composites that were stitched together using the scan feature on EVOS. MC refers to maternal channel. The extent of EVT invasion into the mesometrial triangle in acute (B) and chronic (C) infection. Values in each graph represent the mean ± SD of six biological replicates from two independent experiments. Data were analyzed by one-way ANOVA and Tukey tests.

we measured the mRNA expression of these cytokines within the mesometrial tissue of animals in the chronic infection groups. Tissues from acutely infected animals were not available for analysis. We found no difference in mRNA levels of any of these cytokines among control and *Pg*-infected animals (Supplementary Figure S9).

TNF-α is particularly known for inhibiting EVT invasion in vivo [14]. Therefore, we assessed the in situ location of TNF-positive cells in the mesometrial triangle of animals from both the acute and chronic cohort. We performed dual staining of TNF and uterine NK cell marker (ANK1), EVT marker (KRT7), or macrophage marker (CD68) in control and *Pg*-positive specimens (Supplementary Figure S10A). We focused on these cell types since they are known sources of TNF during normal and/or pathologic pregnancy [11, 49, 50]. TNF-positive cells were mainly found around the spiral arteries in the periphery of the mesometrial triangle (Supplementary Figure S10A). Costaining with ANK1 confirmed that the majority of these cells were uterine NK cells in all treatment groups (Supplementary Figure S10B). Intraluminal EVT positive for TNF were occasionally detected in mesometrial sections of all groups (Supplementary Figure S10C). TNF-positive macrophages (CD68 + cells) were not detected in mesometrial tissues from the acute cohort or in control animals from the chronic cohort. However, TNF+ CD68 cells were identified in mesomterial tissues positive for W83 or A7436, usually in association with uterine NK cells and TNF negative CD68 cells (Supplementary Figure S10D).

We measured gene expression of TGF-β superfamily members: TGF-β1 (*Tgfb1*), follistatin-related protein 3 (*Fstl3*), and activin A (*Inhba*) since these mediators can also affect decidualization and/or modulate EVT invasion. FSTL3 and TGF-β1, in particular, inhibit EVT invasion [51], whereas activin A, which is made up of two inhibin beta-A subunits, enhances decidualization and EVT invasion (Figure 4) [52–54]. There was no difference in mRNA levels of *Tgfb1* and *Fstl3* among the groups (Figure 4). However, *Inhba* expression was significantly reduced in tissues from dams seropositive for A7436 ($P < 0.02$). We next examined the in situ location of these mediators in the acute and chronic cohort by immunohistology (Figure 5). Both TGFB1 and inhibin beta A were detected in mesometrial stromal cells. FSLT3, which functionally blocks activin A signaling [55], was detected in spiral arteries in all groups, particularly in EVT within the decidual arterial lumen or vessel wall. (Supplementary Figure S11). The proportion of EVT positive for FSLT3 was greater in tissues infected with A7436 than in control

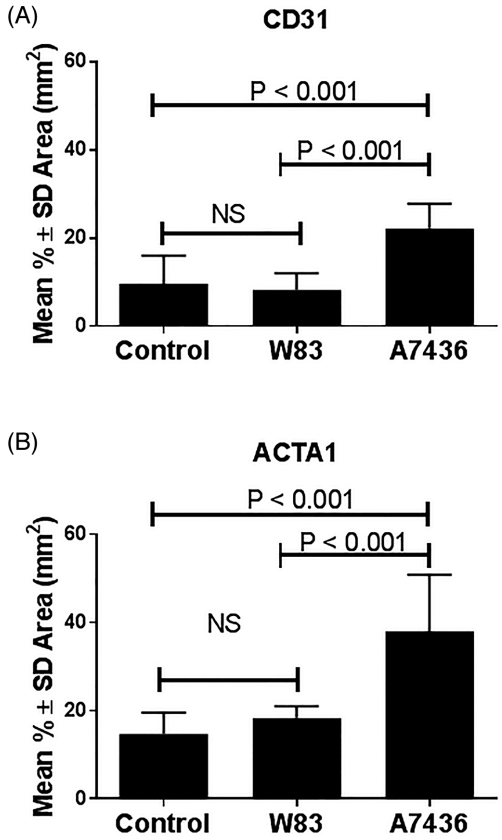

Figure 3. *Pg* strain-dependent effects on spiral artery remodeling at GD18 in the chronically infected cohort. Endothelial cells (A) were identified with antibody to CD31 and vascular smooth muscle cells (B) were identified with antibody to ACTA1. Values represent the mean ± SD of six biological replicates from two independent experiments. Data were analyzed by one way ANOVA and Tukey tests.

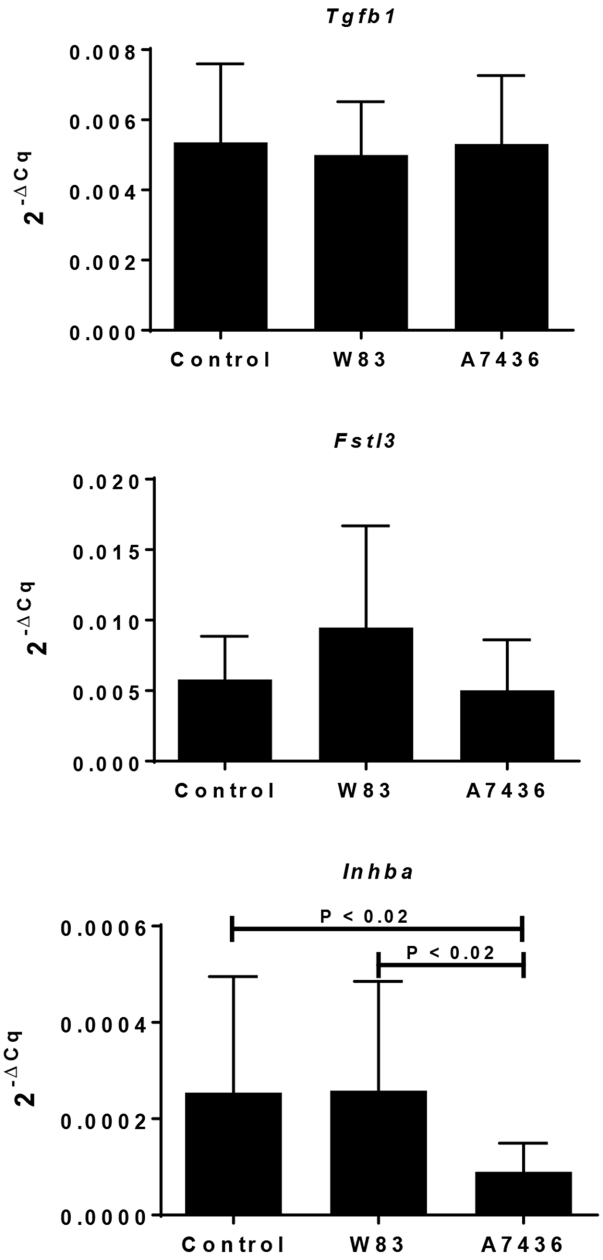

Figure 4. Gene expression of TGFB1 superfamily members in the metrial triangle of sham control and dams chronically infected with *Pg*. Values reflect the mean $2^{-\Delta Cq}$ ± SD relative gene expression of 12 biological replicates obtained from two independent experiments. The corresponding *Actb* Cq was used as the reference gene for each sample. Data were analyzed by Kruskall–Wallis followed by Dunn multiple comparison's test.

or W83-infected tissues (Figure 6; Supplementary Figure S11) ($P < 0.001$).

DISCUSSION

The underlying mechanisms that lead to DDP are unknown, but there is emerging evidence that abnormalities of the endometrium and inner myometrium before or during the early stages of placentation are involved in the disease process [1]. Given that bacteria including *Pg* can be found in the decidua/basal plate [15–17, 22, 25, 56], and that *Pg*, in particular, is implicated in adverse pregnancy outcomes [57], we wanted to determine if *Pg* could promote DDP. Using a rat model of infection, we were able to establish that *Pg* reaches the maternal–fetal interface and induces lesions consistent with DDP including increased fetal loss, albeit in a microbial strain-dependent manner.

We observed different forms of vascular injury in *Pg*-infected tissues. Although rare, atherosis-like pathology was exclusive to A7436-infected tissues in the chronic cohort group. Atherosis is usually present in spiral arteries that failed to undergo physiologic transformation [58, 59], and the vessels that contained this lesion in A7436-infected animals were only partially transformed. Another more common lesion that was observed in both W83 and A7436 chronically infected tissues was thrombosis with coagulative necrosis, which is associated with ischemia [43]. This lesion may be the end result of a chronic insidious inflammatory process initiated by *Pg* infection [41, 60]. *Pg* has been shown to activate arterial endothelial cells, increasing the expression of cell adhesion molecules that attract leukocytes and enhanced pro-coagulant responses in these cells [41, 61]. Arteritis found in acutely infected animals as well as TNF expressing macrophages found in chronically infected animals are indicative of mesometrial vascular inflammation. The increased vascular necrosis in chronically infected animals may be the result of *Pg*-induced vascular damage coupled with pregnancy-enhanced

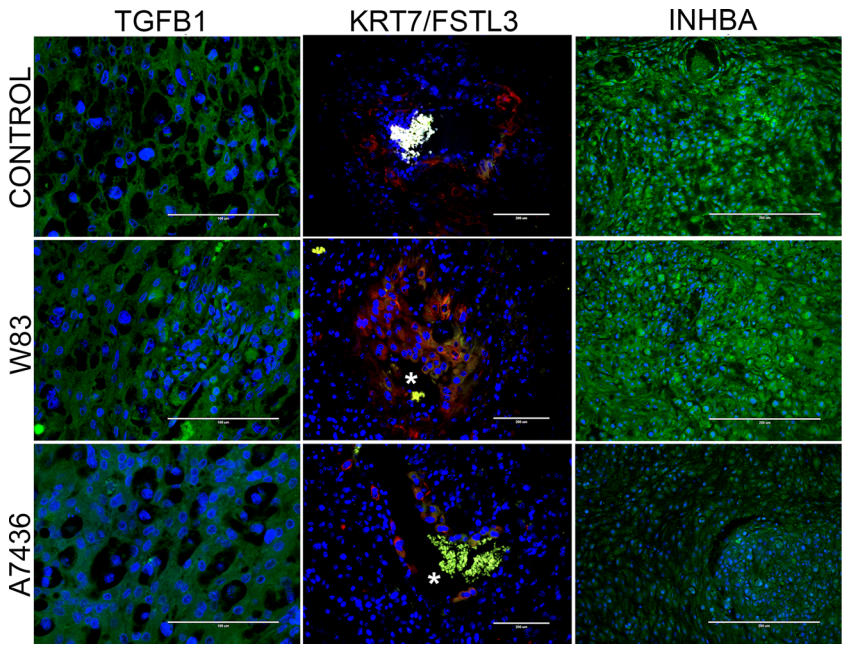

Figure 5. Representative images of TGFB1 (green), cytokeratin-7 (KRT7, red)/follistatin-related protein 3 (FSTL3, green), and inhibin beta A (green) staining in the mesometrial triangle of control, W83, and A7436 groups. "∗" indicates the presence of autofluorescent red blood cells within the vessel lumen. Scale bar in stained sections is equal to 100 μm (TGFB1) or 200 μm (KRT7/FSTL3, INHBA).

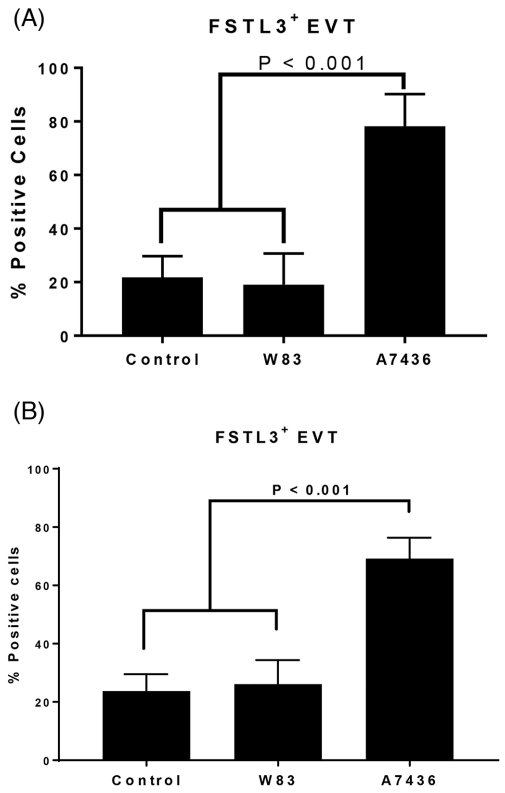

Figure 6. The percentage of FSLT3-positive EVT in the mesometrial arterioles of control, and *Pg*-antigen positive groups from the acute (A) and chronic (B) cohorts. Values in each graph represent the mean ± SD of five biological replicates from two independent experiments. Data were analyzed by one-way ANOVA and Tukey test.

platelet aggregation, vascular constriction, and thrombin formation [62]. Since this lesion was common in W83-infected tissues, the pathogenesis of mesometrial vascular necrosis with thrombosis does not appear to be directly related to *Pg*-induced DDP. However, as suggested by mesometrial/decidual vascular lesions in fetal resorptions, this form of vascular damage may play a role in placental defects [63] and fetal morbidity and mortality [64].

A common lesion in animals acutely and chronically infected with A7436 was the dramatic reduction in EVT. Since A7436 was primarily found in, or associated with, decidual/mesometrial stromal cells, we measured the expression of various mediators known to affect EVT invasion. There was no significant difference in the overall expression of cytokines among the groups. While this may be a true reflection of *Pg* infection within the stroma, we cannot rule out the possibility that some of the specimens that were examined were not infected and could have produced a spurious result. Despite this limitation, *Inhba* expression was significantly decreased in specimens from A7436-infected dams that had DDP. It is worth noting that Activin A (comprised of two inhibin beta A protein subunits) facilitates spiral artery remodeling by several mechanisms. Activin A promotes decidualization of human endometrial stroma [65] and enhances EVT invasion through induction of matrix metalloproteinase 2 (MMP-2) expression [52]. In contrast, TGF-β and follistatin-related protein 3 can interfere with this process. TGF-β indirectly impedes EVT invasion by inhibiting MMP-2 activity [9], whereas follistatin-related protein 3 directly antagonizes Activin A function in targeted cells via paracrine communication [55]. FSLT3 (also known as FLRG) in particular is localized to decidual and placental blood vessels in humans, and it has been postulated that it mediates Activin A signaling in blood vessels [66]. While the overall expression levels of mesometrial *Tgfb1* and *fslt3* were similar among control and *Pg* groups, we found that the proportion of FSLT3-positive EVT was greater in the spiral arteries of A7436-infected animals. Thus, FSLT3 may be further aggravating an already

compromised physiologic process of spiral artery remodeling. Given the in situ location of *Pg* in the mesometrial stroma, we propose that *Pg* A7436 may be exerting its effects on mesometrial stromal cells with downstream consequences on the regulation of activin A expression and function at the maternal–fetal interface. As a consequence, EVT invasion into the uterine tissue and spiral arteries is reduced and the spiral arteries are not adequately remodeled.

Decidual vasculopathy is most commonly defined as the presence of foam filled macrophages and fibrinoid necrosis within the vessel wall, but perivascular inflammatory cell infiltration with thrombosis and medial hypertrophy have also been reported [2, 64]. In preeclamptic women, fetal morbidity and mortality is correlated with the degree of decidual vasculopathy, particularly if it includes thrombosis [64]. We observed a similar effect in our study. For example, both W83- and A7436-infected animals had similar rates of mesometrial/decidual vascular necrosis, but A7436 also had reduced spiral artery remodeling and atherosis-like pathology. These lesions probably had a cumulative effect that contributed to poorer fetal outcomes (i.e., smaller placenta and increased number of fetal resorptions).

The oral inoculation protocol that was used in this study induces a strong IgG response to *Pg* that does not confer protection against periodontal destruction [40]. In pregnant mice, the development of high IgG titers to *Pg* was seen in dams with intrauterine infection and fetal growth restriction [28]. We therefore used serology as a screening tool to identify animals with likely microbial dissemination. Consistent with previous reports [40], none of the *Pg*-inoculated dams had *Pg*-specific IgM. Although we limited our analysis to Pg positive specimens from dams with a strong IgG response to *Pg*, we did not see fetal growth restriction. This may be partly related to host-specific factors since we used SD rats, whereas other studies used mice or Wistar rats [27–29]. Alternatively, our methodology may have affected our outcome since we used repeated oral inoculations to produce chronic infection [40] rather than use subcutaneous inoculation [29] or inoculation of molar pulp chambers [30] to establish infection.

It is not surprising that infection with W83 and A7436 would not produce identical outcomes. *Pg* strain-dependent effects on disease have been observed in both epidemiologic and experimental infection studies [36, 67, 68]. The differences between W83 and A7436 may be due in part to microbial diversity and its effect on host responses rather than differences in colonization since both seroconversion rates and the in situ location of *Pg* within the utero-placental tissue was similar.

Our intent was to determine if *Pg* infection would induce DDP. In this study, we established for the first time that infection with *Pg* can impair the physiologic remodeling of spiral arteries, producing lesions consistent with DDP, and that *Pg*-mediated DDP may involve stromal cell dysfunction. In addition, we demonstrate that *Pg*-mediated DDP is microbial strain dependent, which may explain some of the discrepancies between the presence of periodontal disease in women and risk for adverse pregnancy outcome [69].

Supplementary data

Supplementary data are available at *BIOLRE* online.

Supplementary Figure S1. Representative images of stromal necrosis (A), arteritis in acute cohort (B), arteritis in a partially transformed artery in the chronic cohort (C), and coagulative necrosis (D) in H&E-stained mesometrial tissues collected at GD18. Arrows highlight regions within magnified inserts in A (pyknotic nuclei), B (inflammatory cells attached and invading the vessel wall), and C (aggregate of leukocytes in the vessel wall between fibrinoid deposits and necrotic vessel wall). Intraluminal EVT in panel C are indicated by white arrows. Black arrows in (D) demarcate necrotic thrombosed vessels. Scale bars are equivalent to 200 μm.

Supplementary Figure S2. Representative utero-placental sections from control (A), W83 (B), and A7436 (C) positive tissues that were used for placental area measurements. Picture composites are stitched images obtained at 4× magnification. A calibrated image taken at 4× was used to determine scale for each composite image with Image J software. Scale bar = 5 mm.

Supplementary Figure S3. Demonstration of *Sry1* and *Actb* gene amplification in formalin fixed paraffin embedded placental specimens. '+' = positive control DNA obtained from male rat (white M label in gel image). M (black font) = DNA ladder.

Supplementary Figure S4. Corresponding controls for *Pg*-stained metrial sections. (A) Isotype control and (B) uninfected control, Blue = DAPI nuclear stain, Green = ActinGreen 488, scale bar is equivalent.

Supplementary Figure S5. Absorbance values of *Pg*-specific IgG in sera collected from control and *Pg*-infected dams at gestation day 18. Neg = pooled sera from uninfected rats. Pos = pooled sera from infected rats. Data points within the dotted line indicate dams that seroconverted and their tissues were used for downstream analysis.

Supplementary Figure S6. Representative images of H&E-stained chorionic plate (CP), yolk sac (YS), andumbilical cord (UC) sections from control (A), W83 (B), and A7436 (C) positive groups. Scale bars are equivalent to 1000 μm.

Supplementary Figure S7. Representative images of fetal resorptions in control and *Pg*-infected animals. Left panel figures are composites of stitched images obtained at 4× magnification. M = mesometrium and PL = placenta. Black arrows demarcate magnified images of corresponding mesometrium (scale bar = 200 μm) and placenta (scale bar = 100 μm).

Supplementary Figure S8. Representative images of EVT density (cytokeratin positive in green), endothelial cells (CD31, red), and vascular smooth muscle cell (α-actin, green) in the metrial triangle of control, W83- and A7436-infected dams. Scale bars are equal to 200 μm for most images except cytokeratin-7 control and A7436 in which scale bar is equal to 400 μm.

Supplementary Figure S9. Cytokine gene expression in the metrial triangle of control and chronically infected *Pg* dams. Values reflect the mean ± SD relative gene expression (n = 12 from 2 separate experiments) with the corresponding *Actb* Cq used as reference for each sample.

Supplementary Figure S10. Distribution of TNF-positive cells in the mesometrial triangle of control and/or *Pg*-positive specimens. Panel A and its corresponding isotype control are stitched composite images taken at 10× magnification. (A) White arrows indicate TNF+ cells (red) around spiral arteries. Corresponding isotype control reveals the pattern of autofluorescent red blood cells (red) in mesometrial vasculature. Nuclei are stained with DAPI (blue). Colocalization of TNF+ : uterine NK cells (B), EVT (C), and CD68 + macrophages (D). Scale bar = 100 μm (B and C, 200 μm in D).

Supplementary Figure S11. Colocalization of follistatin like 3 (FSLT3, green) and cytokeratin-7 (KRT7, red) in metrial tissue sections from control and *Pg*-infected dams. Scale bar is equivalent to 200 μm. "*" indicates spiral arterial lumen.

Supplementary Table S1. Antibodies used for immunohistology or ELISA.

Supplementary Table S2. Primer sequences used for determination of fetal sex.

References

1. Khong Y, Brosens I. Defective deep placentation. *Best Pract Res Clin Obstet Gynaecol* 2011; **25**(3):301–311.
2. Kim YM, Chaemsaithong P, Romero R, Shaman M, Kim CJ, Kim JS, Qureshi F, Jacques SM, Ahmed AI, Chaiworapongsa T, Hassan SS, Yeo L et al. The frequency of acute atherosis in normal pregnancy and preterm labor, preeclampsia, small-for-gestational age, fetal death and midtrimester spontaneous abortion. *J Matern Fetal Neonatal Med* 2015; **28**:2001–2009.
3. Craven CM, Morgan T, Ward K. Decidual spiral artery remodelling begins before cellular interaction with cytotrophoblasts. *Placenta* 1998; **19**(4):241–252.
4. Conrad KP, Rabaglino MB, Post Uiterweer ED. Emerging role for dysregulated decidualization in the genesis of preeclampsia. *Placenta* 2017; **60**:119–129.
5. Whitley GS, Cartwright JE. Cellular and molecular regulation of spiral artery remodelling: lessons from the cardiovascular field. *Placenta* 2010; **31**(6):465–474.
6. Rabaglino MB, Post Uiterweer ED, Jeyabalan A, Hogge WA, Conrad KP. Bioinformatics approach reveals evidence for impaired endometrial maturation before and during early pregnancy in women who developed preeclampsia. *Hypertension* 2015; **65**(2):421–429.
7. Dimitriadis E, White CA, Jones RL, Salamonsen LA. Cytokines, chemokines and growth factors in endometrium related to implantation. *Hum Reprod Update* 2005; **11**(6):613–630.
8. Jones RL, Salamonsen LA, Zhao YC, Ethier JF, Drummond AE, Findlay JK. Expression of activin receptors, follistatin and betaglycan by human endometrial stromal cells; consistent with a role for activins during decidualization. *Mol Hum Reprod* 2002; **8**(4):363–374.
9. Graham CH, Lala PK. Mechanism of control of trophoblast invasion in situ. *J Cell Physiol* 1991; **148**(2):228–234.
10. Sharma S, Godbole G, Modi D. Decidual control of trophoblast invasion. *Am J Reprod Immunol* 2016; **75**(3):341–350.
11. Otun HA, Lash GE, Innes BA, Bulmer JN, Naruse K, Hannon T, Searle RF, Robson SC. Effect of tumour necrosis factor-alpha in combination with interferon-gamma on first trimester extravillous trophoblast invasion. *J Reprod Immunol* 2011; **88**(1):1–11.
12. Winship AL, Koga K, Menkhorst E, Van Sinderen M, Rainczuk K, Nagai M, Cuman C, Yap J, Zhang JG, Simmons D, Young MJ, Dimitriadis E. Interleukin-11 alters placentation and causes preeclampsia features in mice. *Proc Natl Acad Sci USA* 2015; **112**(52):15928–15933.
13. Peng J, Monsivais D, You R, Zhong H, Pangas SA, Matzuk MM. Uterine activin receptor-like kinase 5 is crucial for blastocyst implantation and placental development. *Proc Natl Acad Sci USA* 2015; **112**(36):E5098–E5107.
14. Cotechini T, Komisarenko M, Sperou A, Macdonald-Goodfellow S, Adams MA, Graham CH. Inflammation in rat pregnancy inhibits spiral artery remodeling leading to fetal growth restriction and features of preeclampsia. *J Exp Med* 2014; **211**(1):165–179.
15. Swati P, Thomas B, Vahab SA, Kapaettu S, Kushtagi P. Simultaneous detection of periodontal pathogens in subgingival plaque and placenta of women with hypertension in pregnancy. *Arch Gynecol Obstet* 2012; **285**(3):613–619.
16. Chaparro A, Blanlot C, Ramirez V, Sanz A, Quintero A, Inostroza C, Bittner M, Navarro M, Illanes SE. *Porphyromonas gingivalis*, *Treponema denticola* and toll-like receptor 2 are associated with hypertensive disorders in placental tissue: a case-control study. *J Periodontal Res* 2013; **48**:802–809.
17. Barak S, Oettinger-Barak O, Machtei EE, Sprecher H, Ohel G. Evidence of periopathogenic microorganisms in placentas of women with preeclampsia. *J Periodontol* 2007; **78**(4):670–676.
18. Keelan JA, Wong PM, Bird PS, Mitchell MD. Innate inflammatory responses of human decidual cells to periodontopathic bacteria. *Am J Obstet Gynecol* 2010; **202**(5):471.e1–471.e11.
19. Reyes L, Herrera D, Kozarov E, Rolda S, Progulske-Fox A. Periodontal bacterial invasion and infection: contribution to atherosclerotic pathology. *J Periodontol* 2013; **84**(4-s):S30–S50.
20. Chaparro A, Sanz A, Quintero A, Inostroza C, Ramirez V, Carrion F, Figueroa F, Serra R, Illanes SE. Increased inflammatory biomarkers in early pregnancy is associated with the development of pre-eclampsia in patients with periodontitis: a case control study. *J Periodontal Res* 2013; **48**(3):302–307.
21. Moura da Silva G, Coutinho SB, Piscoya MD, Ximenes RA, Jamelli SR. Periodontitis as a risk factor for preeclampsia. *J Periodontol* 2012; **83**(11):1388–1396.
22. Leon R, Silva N, Ovalle A, Chaparro A, Ahumada A, Gajardo M, Martinez M, Gamonal J. Detection of *Porphyromonas gingivalis* in the amniotic fluid in pregnant women with a diagnosis of threatened premature labor. *J Periodontol* 2007; **78**(7):1249–1255.
23. Dasanayake AP, Boyd D, Madianos PN, Offenbacher S, Hills E. The association between *Porphyromonas gingivalis*-specific maternal serum IgG and low birth weight. *J Periodontol* 2001; **72**(11):1491–1497.
24. Sasahara J, Kikuchi A, Takakuwa K, Sugita N, Abiko Y, Yoshie H, Tanaka K. Antibody responses to *Porphyromonas gingivalis* outer membrane protein in the first trimester. *Aust N Z J Obstet Gynaecol* 2009; **49**(2):137–141.
25. Vanterpool SF, Been JV, Houben ML, Nikkels PG, De Krijger RR, Zimmermann LJ, Kramer BW, Progulske-Fox A, Reyes L. *Porphyromonas gingivalis* within placental villous mesenchyme and umbilical cord stroma is associated with adverse pregnancy outcome. *PLoS One* 2016; **11**(1):e0146157.
26. Katz J, Chegini N, Shiverick KT, Lamont RJ. Localization of *P. gingivalis* in preterm delivery placenta. *J Dent Res* 2009; **88**(6):575–578.
27. Lin D, Smith MA, Elter J, Champagne C, Downey CL, Beck J, Offenbacher S. *Porphyromonas gingivalis* infection in pregnant mice is associated with placental dissemination, an increase in the placental Th1/Th2 cytokine ratio, and fetal growth restriction. *Infect Immun* 2003; **71**(9):5163–5168.
28. Lin D, Smith MA, Champagne C, Elter J, Beck J, Offenbacher S. *Porphyromonas gingivalis* infection during pregnancy increases maternal tumor necrosis factor alpha, suppresses maternal interleukin-10, and enhances fetal growth restriction and resorption in mice. *Infect Immun* 2003; **71**(9):5156–5162.
29. Michelin M, Teixeira S, Ando-Suguimoto E, Lucas S, Mayer M. *Porphyromonas gingivalis* infection at different gestation periods on fetus development and cytokines profile. *Oral Dis* 2012; **18**(7):648–654.
30. Ao M, Miyauchi M, Furusho H, Inubushi T, Kitagawa M, Nagasaki A, Sakamoto S, Kozai K, Takata T. Dental infection of *Porphyromonas gingivalis* induces preterm birth in mice. *PLoS One* 2015; **10**(8):e0137249.
31. Kim CJ, Romero R, Chaemsaithong P, Chaiyasit N, Yoon BH, Kim YM. Acute chorioamnionitis and funisitis: definition, pathologic features, and clinical significance. *Am J Obstet Gynecol* 2015; **213**(4):S29–S52.
32. Brosens I, Pijnenborg R, Vercruysse L, Romero R. The "Great Obstetrical Syndromes" are associated with disorders of deep placentation. *Am J Obstet Gynecol* 2011; **204**(3):193–201.
33. Kim YM, Chaiworapongsa T, Gomez R, Bujold E, Yoon BH, Rotmensch S, Thaler HT, Romero R. Failure of physiologic transformation of the spiral arteries in the placental bed in preterm premature rupture of membranes. *Am J Obstet Gynecol* 2002; **187**(5):1137–1142.
34. Inaba H, Kuboniwa M, Bainbridge B, Yilmaz O, Katz J, Shiverick KT, Amano A, Lamont RJ. *Porphyromonas gingivalis* invades human trophoblasts and inhibits proliferation by inducing G1 arrest and apoptosis. *Cell Microbiol* 2009; **11**(10):1517–1532.
35. Riewe SD, Mans JJ, Hirano T, Katz J, Shiverick KT, Brown TA, Lamont RJ. Human trophoblast responses to *Porphyromonas gingivalis* infection. *Mol Oral Microbiol* 2010; **25**(4):252–259.
36. Belanger M, Reyes L, von Deneen K, Reinhard MK, Progulske-Fox A, Brown MB. Colonization of maternal and fetal tissues by Porphyromonas

gingivalis is strain-dependent in a rodent animal model. *Am J Obstet Gynecol* 2008; **199**(1):86.e1–86.e7.
37. Romero R, Kusanovic JP, Chaiworapongsa T, Hassan SS. Placental bed disorders in preterm labor, preterm PROM, spontaneous abortion and abruptio placentae. *Best Pract Res Clin Obstet Gynaecol* 2011; **25**(3):313–327.
38. Soares MJ, Chakraborty D, Karim Rumi MA, Konno T, Renaud SJ. Rat placentation: An experimental model for investigating the hemochorial maternal-fetal interface. *Placenta* 2012; **33**(4):233–243.
39. Vercruysse L, Caluwaerts S, Luyten C, Pijnenborg R. Interstitial trophoblast invasion in the decidua and mesometrial triangle during the last third of pregnancy in the rat. *Placenta* 2006; **27**(1):22–33.
40. Verma RK, Bhattacharyya I, Sevilla A, Lieberman I, Pola S, Nair M, Wallet SM, Aukhil I, Kesavalu L. Virulence of major periodontal pathogens and lack of humoral immune protection in a rat model of periodontal disease. *Oral Dis* 2010; **16**(7):686–695.
41. Rodrigues PH, Reyes L, Chadda AS, Belanger M, Wallet SM, Akin D, Dunn W, Jr., Progulske-Fox A. Porphyromonas gingivalis strain specific interactions with human coronary artery endothelial cells: a comparative study. *PLoS One* 2012; **7**(12):e52606.
42. Allam AB, von Chamier M, Brown MB, Reyes L. Immune profiling of BALB/C and C57BL/6 mice reveals a correlation between Ureaplasma parvum-Induced fetal inflammatory response syndrome-like pathology and increased placental expression of TLR2 and CD14. *Am J Reprod Immunol* 2014; **71**(3):241–251.
43. Adigun R, Bhimji SS. Necrosis, cell (liquefactive, coagulative, caseous, fat, fibrinoid, and gangrenous). *StatPearls*. [Internet]. Treasure Island (FL): https://www.ncbi.nlm.nih.gov/books/NBK430935. Accessed 12 March 2018.
44. Kesavalu L, Sathishkumar S, Bakthavatchalu V, Matthews C, Dawson D, Steffen M, Ebersole JL. Rat model of polymicrobial infection, immunity, and alveolar bone resorption in periodontal disease. *Infect Immun* 2007; **75**(4):1704–1712.
45. Schmittgen TD, Livak KJ. Analyzing real-time PCR data by the comparative CT method. *Nat Protoc* 2008; **3**(6):1101–1108.
46. Turner ME, Martin C, Martins AS, Dunmire J, Farkas J, Ely DL, Milsted A. Genomic and expression analysis of multiple Sry loci from a single Rattus norvegicus Y chromosome. *BMC Genet* 2007; **8**(1):11.
47. Harris LK. Review: Trophoblast-vascular cell interactions in early pregnancy: how to remodel a vessel. *Placenta* 2010; **31**(Suppl):S93–S98.
48. Prutsch N, Fock V, Haslinger P, Haider S, Fiala C, Pollheimer J, Knofler M. The role of interleukin-1beta in human trophoblast motility. *Placenta* 2012; **33**(9):696–703.
49. Pijnenborg R, Vercruysse L, Hanssens M. The uterine spiral arteries in human pregnancy: facts and controversies. *Placenta* 2006; **27**(9-10):939–958.
50. Staff AC, Dechend R, Pijnenborg R. Learning from the placenta: acute atherosis and vascular remodeling in preeclampsia-novel aspects for atherosclerosis and future cardiovascular health. *Hypertension* 2010; **56**(6):1026–1034.
51. Graham CH, Lala PK. Mechanisms of placental invasion of the uterus and their control. *Biochem Cell Biol* 1992; **70**(10-11):867–874.
52. Jones RL, Stoikos C, Findlay JK, Salamonsen LA. TGF-beta superfamily expression and actions in the endometrium and placenta. *Reproduction* 2006; **132**(2):217–232.
53. Jones RL, Findlay JK, Farnworth PG, Robertson DM, Wallace E, Salamonsen LA. Activin A and inhibin A differentially regulate human uterine matrix metalloproteinases: potential interactions during decidualization and trophoblast invasion. *Endocrinology* 2006; **147**(2):724–732.
54. Jones RL, Salamonsen LA, Findlay JK. Potential roles for endometrial inhibins, activins and follistatin during human embryo implantation and early pregnancy. *Trends Endocrinol Metab* 2002; **13**(4):144–150.
55. Schneyer A, Sidis Y, Xia Y, Saito S, del Re E, Lin HY, Keutmann H. Differential actions of follistatin and follistatin-like 3. *Mol Cell Endocrinol* 2004; **225**(1-2):25–28.
56. Stout MJ, Conlon B, Landeau M, Lee I, Bower C, Zhao Q, Roehl KA, Nelson DM, Macones GA, Mysorekar IU. Identification of intracellular bacteria in the basal plate of the human placenta in term and preterm gestations. *Am J Obstet Gynecol* 2013; **208**(3):226.e1–226.e7.
57. Reyes L, Phillips P, Wolfe B, Golos TG, Walkenhorst M, Progulske-Fox A, Brown M. Porphyromonas gingivalis and adverse pregnancy outcome. *J Oral Microbiol* 2017; **9**(1):1374153.
58. Staff AC, Johnsen GM, Dechend R, Redman CW. Preeclampsia and uteroplacental acute atherosis: immune and inflammatory factors. *J Reprod Immunol* 2014; **101–102**:120–126.
59. Labarrere CA, DiCarlo HL, Bammerlin E, Hardin JW, Kim YM, Chaemsaithong P, Haas DM, Kassab GS, Romero R. Failure of physiologic transformation of spiral arteries, endothelial and trophoblast cell activation, and acute atherosis in the basal plate of the placenta. *Am J Obstet Gynecol* 2017; **216**(3):287.e1–287.e16.
60. Roth GA, Moser B, Huang SJ, Brandt JS, Huang Y, Papapanou PN, Schmidt AM, Lalla E. Infection with a periodontal pathogen induces procoagulant effects in human aortic endothelial cells. *J Thromb Haemost* 2006; **4**(10):2256–2261.
61. Roth GA, Aumayr K, Giacona MB, Papapanou PN, Schmidt AM, Lalla E. Porphyromonas gingivalis infection and prothrombotic effects in human aortic smooth muscle cells. *Thromb Res* 2009; **123**(5):780–784.
62. Hayashi M, Inoue T, Hoshimoto K, Hirabayashi H, Negishi H, Ohkura T. The levels of five markers of hemostasis and endothelial status at different stages of normotensive pregnancy. *Acta Obstet Gynecol Scand* 2002; **81**(3):208–213.
63. Fitzgerald B, Shannon P, Kingdom J, Keating S. Rounded intraplacental haematomas due to decidual vasculopathy have a distinctive morphology. *J Clin Pathol* 2011; **64**(8):729–732.
64. Stevens DU, Al-Nasiry S, Bulten J, Spaanderman MEA. Decidual vasculopathy in preeclampsia: Lesion characteristics relate to disease severity and perinatal outcome. *Placenta* 2013; **34**(9):805–809.
65. Jones RL, Salamonsen LA, Findlay JK. Activin A promotes human endometrial stromal cell decidualization in vitro. *J Clin Endocrinol Metab* 2002; **87**(8):4001–4004.
66. Ciarmela P, Florio P, Toti P, Franchini A, Maguer-Satta V, Ginanneschi C, Ottaviani E, Petraglia F. Human placenta and fetal membranes express follistatin-related gene mRNA and protein. *J Endocrinol Invest* 2003; **26**(7):641–645.
67. Igboin CO, Griffen AL, Leys EJ. Porphyromonas gingivalis strain diversity. *J Clin Microbiol* 2009; **47**(10):3073–3081.
68. Baker PJ, Dixon M, Evans RT, Roopenian DC. Heterogeneity of Porphyromonas gingivalis strains in the induction of alveolar bone loss in mice. *Oral Microbiol Immunol* 2000; **15**(1):27–32.
69. Sanz M, Kornman K. Working group 3 of joint EFP/AAP workshop. Periodontitis and adverse pregnancy outcomes: consensus report of the Joint EFP/AAP Workshop on Periodontitis and Systemic Diseases. *J Clin Periodontol* 2013; **40**(Suppl 14):S164–169.